Cell, Vol. 81, 991–1002, June 30, 1995, Copyright © 1995 by Cell Press

The Crystal Structure of an All-RNA Hammerhead Ribozyme: A Proposed Mechanism for RNA Catalytic Cleavage

William G. Scott, John T. Finch, and Aaron Klug
Medical Research Council
Laboratory of Molecular Biology
Hills Road
Cambridge CB2 2QH
England

Summary

We have solved the crystal structure of an all-RNA hammerhead ribozyme having a single 2′-O-methyl cytosine incorporated at the active site to prevent cleavage. The conditions used differ from those in another recent solution in four significant ways: first, it is an all-RNA ribozyme rather than a DNA–RNA hybrid; second, the connectivity of the ribozyme backbone strands is different; third, the crystals were grown in the presence of a much lower concentration of salt; and fourth, the crystal packing scheme is very different. Nevertheless, the three-dimensional structure of the all-RNA hammerhead ribozyme is similar to the previous structure. Five potential Mg(II)-binding sites are identified, including one positioned near the ribozyme catalytic pocket. Upon this basis, as well as upon comparisons with the metal-binding sites in the structurally homologous uridine turn of $tRNA^{Phe}$, we propose a mechanism for RNA catalytic cleavage.

Introduction

The unexpected discovery that RNA can act as an enzyme has inspired research efforts dedicated not only to understanding the mechanisms of RNA-catalyzed cleavage and ligation reactions (reviewed by Cech, 1990; Gopalan et al., 1994; Symons, 1992), but also to developing ribozyme-based therapies targeted against RNA viruses and oncogene messenger RNA (Barinaga, 1993; Sullenger and Cech, 1993). The role of RNA enzymes in primordial life forms is also of wide interest (Gesteland and Atkins, 1993). Although much has been learned about the enzymology and molecular biology of ribozymes, a detailed understanding of the three-dimensional structures of RNA enzymes is only now emerging. The structures of yeast $tRNA^{Phe}$ both before and after cleavage in the presence of Pb^{2+} were described over a decade ago (Brown et al., 1983, 1985); however, the structure of a hammerhead ribozyme bound to a DNA substrate analog was only very recently elucidated (Pley et al., 1994). Complementary to the latter study, we now present the structure of an all-RNA hammerhead ribozyme having a minimal modification at the active site to prevent cleavage.

Hammerhead RNAs are small self-cleaving RNAs that have in common a conserved motif found in several viroids and satellite RNAs that replicate via a rolling circle mechanism. The hammerhead motif consists of three base-paired stems flanking a central core of 15 conserved nucleotides, as depicted in Figure 1A (q.v.; Uhlenbeck, 1987; Ruffner et al., 1990; Symons, 1992). The conserved central bases are essential for ribozyme activity. The mechanism of hammerhead RNA self-cleavage involves one or more catalytic divalent metal ions (such as Mg^{2+}, Ca^{2+}, or Mn^{2+}). As with Pb^{2+}–tRNA (Brown et al., 1983), a metal hydroxide bound specifically to the hammerhead RNA initiates the reaction by abstracting the proton from the 2′-hydroxyl at the cleavage site (Dahm and Uhlenbeck, 1991; Dahm et al., 1993). This metal, or another, also stabilizes the pentacoordinated phosphate intermediate (or transition state), as shown in Figure 1B. In addition, a general acid catalyst may act by donating a proton to the 5′-oxygen leaving group during the phosphodiester cleavage reaction, or a second metal may bind to the leaving oxygen directly (Taira et al., 1990). The cleavage reaction, as in the case of Pb^{2+}–tRNA, generates 5′-hydroxyl and 2′,3′–cyclic phosphate termini at the cleavage site.

The recent crystal structure of a hammerhead RNA enzyme strand bound to a DNA substrate inhibitor (Pley et al., 1994) revealed the three-dimensional folding pattern of the hammerhead ribozyme, including the conformation of and base pairing interactions within the core region. However, this structure of the RNA–DNA complex raised two important questions. First, does the presence of a DNA substrate analog significantly perturb the three-dimensional structure of the ribozyme? Second, does the presence of the DNA substrate or of a high concentration of monovalent salt (2 M Li_2SO_4 or $(NH_4)_2SO_4$) used in the crystallization of the ribozyme account for the absence of any divalent metal ions in the neighborhood of the cleavage site?

Our ribozyme crystal structure addresses these two questions, because it is derived from crystals obtained in a low concentration of salt, and we have crystallized a hammerhead RNA enzyme complexed to an all-RNA substrate analog having a minimal chemical modification to prevent cleavage. We have replaced the 2′-hydroxyl of the cytosine at the cleavage site with a 2′-methoxyl group in an otherwise unaltered substrate RNA (Scott et al., 1995) by use of solid-phase oligoribonucleotide phosphoramidite chemical synthesis (Usman et al., 1987; Gait et al., 1991). In addition, a GUAA tetraloop was placed at the end of stem III in our ribozyme instead of a GAAA tetraloop at the end of stem II of the previous ribozyme, rendering a different phosphate backbone connectivity. Finally, our ribozyme crystallized with a very different set of packing interactions compared with those of the previous crystal structure.

Despite all of these differences, the three-dimensional structure of the all-RNA hammerhead ribozyme is nevertheless quite similar to the previously determined RNA–DNA hybrid ribozyme structure, except for the presence of some additional stabilizing hydrogen-bonding interactions. This result strongly suggests that both crystal struc-

tures must be a close approximation to the true solution structure of an unaltered hammerhead ribozyme. We have attempted to integrate into our description of the structure an explanation as to why many of the 15 conserved nucleotides in the hammerhead ribozyme are critical for maintaining its structural architecture and catalytic activity. In addition, upon the basis of our observations of a single solvent peak, found in the catalytic pocket of both ribozyme molecules in the asymmetric unit of the crystal, which we have identified as magnesium, and upon the basis of homologous metal-binding sites found in tRNA crystals, we are able to propose a possible mechanism for divalent metal ion–mediated hammerhead RNA catalysis.

Results and Discussion

Crystallization and Structure Determination

We screened several different chemically synthesized hammerhead RNA constructs against 48 crystallization conditions to find the best sequences and crystals suitable for X-ray analysis (Scott et al., 1995). The RNA complex that yielded crystals that allowed us to solve the three-dimensional structure consists of a 16 nt enzyme strand and a 25 nt substrate strand as depicted in Figure 1A. The structure of the hammerhead ribozyme–RNA substrate analog complex was solved by isomorphous replacement using two separate 5-bromodeoxyuridine (5-BrdU) substitutions in the enzyme strand of stem I, as described in the Experimental Procedures. Native and anomalous difference derivative data were collected on flash-cooled crystals. The initial electron density map revealed good connectivity for the phosphate backbone that could be traced, but only weak density for many of the individual base pairs was present (Table 1). However, the map was improved substantially by noncrystallographic symmetry averaging and solvent flattening (Figure 2a). Stem I was easily located for the two molecules in the asymmetric unit by using the positions of the two bromine atoms in the derivatives; together with the strong density for the tetraloop on stem III, this provided a convenient landmark for building in the remaining portions of the structure. The two molecules were constructed separately and thus served as a check for internal consistency; the packing scheme for the dimer, described below, confirmed the correct registry for stems II and III. The structure was refined both with and without a noncrystallographic harmonic restraint employed within a simulated annealing protocol in X-PLOR 3.1 (A. T. Brünger; see Experimental Procedures). The resulting refinement statistics are reported in Table 1.

Noncrystallographic 2-Fold Symmetry and Crystal Packing Arrangement

The packing scheme for our crystal structure is very different from that of Pley et al. (1994). There are two (rather than three) molecules in our asymmetric unit, related by a simple 180° rotation such that the blunt end of stem I of one molecule base-stacks against the blunt end of stem II in the other molecule (Figure 2b). This leads to a 5′ to 5′ and 3′ to 3′ pseudocontinuous helical packing scheme, somewhat similar to that found in the catabolite gene activator protein–DNA complex (Schultz et al., 1991), but in our case the crystal lattice contacts themselves are not mediated by helical end-to-end abutting interactions. Rather, the consequence of dimer formation is that the asymmetric unit of the crystal is essentially a closed double-helical loop whose crystallographic packing contacts are mediated through interactions between the tetraloop on stem III and the phosphate backbone of the helical regions of the molecules. The packing scheme therefore

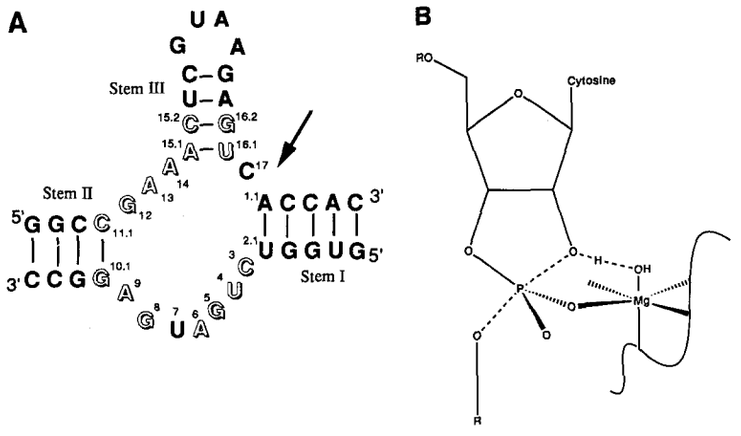

Figure 1. Secondary Structure and Reaction Intermediate of the Hammerhead Ribozyme

(A) The sequence and predicted secondary structure of the hammerhead RNA used to determine the three-dimensional structure reported here. This ribozyme construct, employing a 16 nt enzyme strand (on the bottom) and a 25 nt substrate strand (on the top) is similar to a construct originally described by Uhlenbeck (1987). The letters outlined are absolutely or highly conserved in all hammerhead RNAs (Ruffner et al., 1990). Those that do not form conventional base pairs are believed to be involved in mediating the three-dimensional structure of the hammerhead RNA necessary for catalyzing the self-cleavage reaction. The arrow denotes the self-cleavage site. The helices are labeled stem I, stem II, and stem III. In the naturally occurring self-cleaving hammerhead RNAs, two of the three stems have closed loops. Artificial constructs (such as this one) have only one loop, so that the hammerhead RNA is then divided into arbitrary enzyme and substrate strands.

(B) A putative transition state or intermediate in the reaction pathway of the hammerhead ribozyme cleavage reaction, showing Mg(OH) acting as both a general base catalyst, abstracting a proton from the 2′-hydroxyl of the active site cytosine (at position 17), and as a Lewis acid catalyst, binding to the pro-R phosphate oxygen of the pentacoordinated phosphate at the active site. After Dahm et al. (1993).

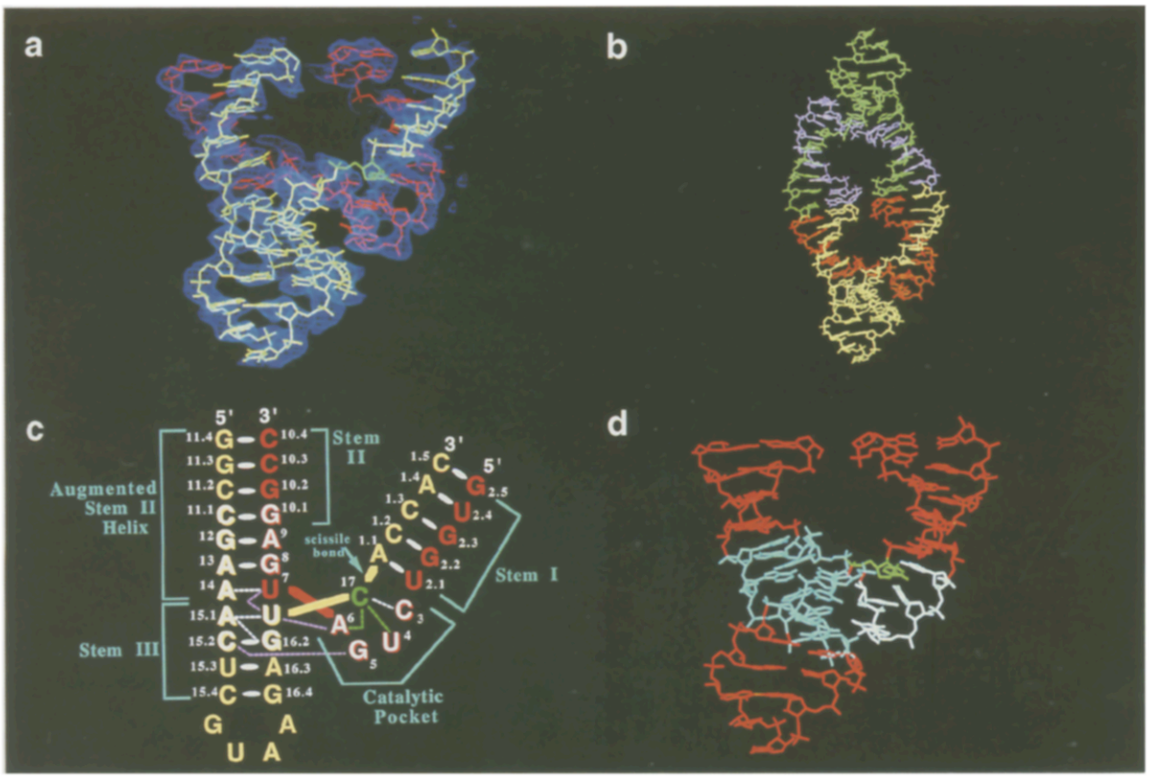

Figure 2. Crystal Structure of the Hammerhead Ribozyme

(a) The noncrystallographic symmetry-averaged and solvent-flattened MIRAS 3.1 Å resolution Fourier electron density map is shown superimposed on the refined structure of the hammerhead RNA. The enzyme strand is shown in red, and the substrate strand is shown in yellow. Before symmetry averaging, most of the electron density for the individual base pairs was not visible.

(b) Illustration of the 5′ to 5′ and 3′ to 3′ packing scheme of the dimer of hammerhead ribozymes in an asymmetric unit of the crystal. The enzyme strands of molecule one and molecule two are shown in red and magenta, respectively, and the substrate strands are likewise shown in yellow and green.

(c) A schematic diagram that shows the structural architecture of the hammerhead RNA. Again the enzyme strand is shown in red and the substrate strand in yellow with the active site cytosine at position 17 highlighted in green. Nonconserved bases are shown as solid letters, and conserved bases are set off as shadowed letters as in Figure 1a. Stems I, II, and III as well as the catalytic pocket formed by the uridine turn and C17 are labeled, as is the augmented stem II helix, as described in the text. Note that the augmented stem II helix stacks directly upon stem III, forming a pseudocontinuous long helix. The phosphate backbone then diverges, as depicted by the yellow strand crossing over the red strand, resulting in C17 being brought into close proximity to the conserved CUGA turn. Watson–Crick and reversed-Hoogsteen bases are denoted by white ovals. Single hydrogen bonds between non-Watson–Crick bases are shown as white broken lines. Single hydrogen bonds between bases and backbone riboses are shown as pink broken lines, and the two aromatic stabilization interactions between C17 and the uridine turn of the catalytic pocket are shown as green broken lines. The scissile bond between C17 and A1.1 is marked with an arrow.

(d) The same view of the refined hammerhead ribozyme as shown in (a) now shows the conserved bases of stem III as well as the 3 bp augmenting helix that joins stem II (top left) to stem–loop III (bottom) highlighted in cyan, the CUGA uridine turn highlighted in white, and the active site cytosine (at position 17) in green. The other helical residues are all shown in red to deemphasize the arbitrary distinction between enzyme and substrate strands, as described in the text.

has the fortuitous consequence that the distortions observed in crystals of short nucleic acid duplexes are likely to be minimized. The helical axes of the dimer are roughly parallel to the 3_1 screw axis in the crystal, thus giving rise to distinct helical arcs in the **c*** direction of the X-ray diffraction pattern. The local contacts mediated by our GUAA tetraloop, however, are somwhat similar to those of the GAAA tetraloop in the previous structure.

Overall Conformation of the Hammerhead Ribozyme

The overall fold of the all-RNA hammerhead ribozyme is roughly γ-shaped, with stem III and its tetraloop forming the apex from which stem I and stem II bifurcate. The hammerhead RNA enzyme–substrate analog complex is depicted in Figure 2a, showing the shorter enzyme and longer substrate analog strands in red and yellow, respectively. Aside from the differences in the connectivity of the phosphodiester backbone and the built-in difference in the position of the tetraloop, the overall fold and conformation of our hammerhead RNA are very similar to that found for the RNA–DNA hybrid ribozyme (Pley et al., 1994). The average root-mean-square deviations between the common residues in the two ribozyme crystal structures are 0.92 Å and 0.77 Å for molecule one and molecule two of our structure compared with molecule two of the previous

Table 1. X-Ray Structure Determination and Refinement

Data Set	Native	BrdU 2.1	BrdU 2.4
Data collection			
Resolution range (Å)	15–3.1	15–3.1	15–4.0
Wavelength (Å)	0.882	0.882	0.882
Unique reflections	6529	6380	2891
Mean redundancy	3.3	7.5	7.1
Reciprocal space coverage (%)	99.9	98.0	95.7
Completeness ($F \geq 2\sigma$) (%)	94.9	93.3	91.0
R_{merge} (%)	8.5	11.0	6.1
Anomalous differences (%)		10.6	11.4
Isomorphous differences (%)		21.5	21.7
Phasing			
Number of sites		2	2
Phasing power		0.7	0.6
R_{Cullis}		0.806	0.89
Figure of Merit		0.601	0.501
Bijvoet pairs completeness (%)		99.5	96.6
NCS 2-Fold Averaging and Solvent Flattening		Crystal Structure Refinement	
Resolution range (Å)	15.0–3.1	R factor (8–3.1 Å)	24.7
Solvent content	0.40	Free R factor (10% of data) (%)	29.3
Number of cycles	18	rmsd bond lengths (Å)	0.018 Å
Correlation coefficient	0.87	rmsd bond angles (degrees)	3.8
Overall figure of merit	0.91	R factor (NCS 2-fold restrained) (%)	26.7

Space group, $P3_121$; cell parameters, a = b = 64.98 Å, c = 138.14 Å, $\alpha = \beta = 90°$, $\gamma = 120°$.

structure, respectively. The average root-mean-square deviation between our two molecules is 0.73 Å, which is only slightly greater than the sum of the mean coordinate errors of these molecules and is essentially insignificant. These results suggest that the presence of an all-DNA substrate analog in the previous hammerhead RNA crystal structure has not disrupted the conformation of the ribozyme.

We describe the hammerhead RNA structure from a point of view that we have found helpful in understanding the relationship between the structure and the function of the ribozyme and that brings out the essence of its design. Stem II and stem III are essentially coaxial, with stem I and the catalytic pocket branching away from this axis. Stem II together with two GA base pairs and an AU base pair forms a so-called augmented stem II helix; stem II forms a standard A-form RNA double helix, and these three additional base pairs (designated domain II by Pley et al. [1994]) extend or augment the helix of stem II, as shown in the schematic diagram of the hammerhead ribozyme design (Figure 2c). The augmented stem II helix stacks directly upon the helix of stem III, forming one long pseudocontinuous, distorted A-form helix. This long helix of course is not actually continuous, because it incorporates a three-strand junction between stem III and the augmented stem II helix. Stacking of the augmented stem II helix upon the stem III helix forces C17, which joins stem III to stem I, outward to stack upon the end of stem I itself and concomitantly into close proximity to the conserved C3–U4–G5–A6 turn. The furanose oxygen of C17 itself stacks on A6, and the base of C17 makes a single hydrogen bond with C3. Now C17 is also the nucleotide at the active site, so its positioning close to this absolutely conserved CUGA turn must be significant.

The CUGA turn was previously designated domain I by Pley et al. (1994), who noted that it is identical in sequence and conformation to the so-called uridine turn found in the anticodon loop of $tRNA^{Phe}$. The four unpaired nucleotides of the hammerhead RNA uridine turn appear to cluster about the cytosine at the cleavage site, suggesting that this uridine turn, together with the active site base, constitutes the catalytic pocket of the ribozyme. Another illustration of the ribozyme–RNA substrate complex, depicted in Figure 2d, shows the four conserved bases forming the uridine turn of the catalytic pocket highlighted in white, and the remaining conserved bases in stem III and the augmented stem II helix are highlighted in cyan. The cytosine at the cleavage site again appears in green.

The Conserved Region Extending Stem II

The three augmenting helical base pairs (or domain II) continue directly from the Watson–Crick G10.1–C11.1 base pair at the base of stem II and consist of two absolutely conserved reversed-Hoogsteen GA base pairs (G12–A9 and A13–G8) followed by a singly hydrogen-bonded AU base pair (A14–U7). Although A14 is absolutely conserved, the U may be replaced with C, G, or A, and the ribozyme will still maintain some catalytic activity (Ruffner et al., 1990). This AU pair of the stem II augmented helix in turn stacks upon the absolutely conserved AU base pair of stem III (A15.1–U16.1). Together with a second, semiconserved Watson–Crick base pair (G15.2–C16.2) in stem III, these base pairs form an imperfect helical duplex region of continuously stacked bases joining

stem II to stem III, as depicted schematically in Figure 2c and in more detail in Figure 3. As we have described above, one of the backbone strands of the long pseudo-continuous helix is broken between U7 and U16.1, where the paths of the phosphodiester backbone strands diverge. Although the active site nucleotide, C17, is linked to U16.1 of stem III, the stacking action of U16.1 upon U7 of the augmented helix expels C17 from the helical region and into the uridine turn of four nucleotides that links stem I to U7 of the augmented stem II helix. Thus, the role of the conserved bases of the augmented stem II helix as it stacks upon the conserved bases of stem III is to force the cleavable nucleotide into the catalytic pocket of the hammerhead ribozyme.

The Conserved Region of Stem III and the Three-Strand Junction

The conserved base pairs in stem III (A15.1–U16.1 and C15.2–G16.2) lie adjacent to the active site C17 and are stacked upon the A14–U7 non-Watson–Crick base pair of the abutting augmented stem II helix, as shown in Figure 2c. The two conserved base pairs of stem III are thus positioned to mediate the three-strand junction among stem I, stem III, and the stem II augmented helix. The A15.1–U16.1 base pair is absolutely conserved, whereas the sequence requirement for the second of these base pairs is less stringent (Ruffner et al., 1990). U7 stacks upon U16.1 of stem III, but the divergent phosphate backbone paths at the three-strand junction are the consequence of different helical conformations in the augmented stem II helix and the abutting stem III.

Although both the A14–U7 and the A15.1–U16.1 pair do not form the usual two hydrogen bonds, they differ from one another in that the A15.1–U16.1 pair has a single hydrogen bond between O4 of U16.1 and the exocyclic amino group of A15.1, whereas the A14–U7 pair is mediated by a single hydrogen bond involving the O2 of U7. The A15.1–U16.1 pair in stem III thus locally broadens the minor groove, whereas the A14–U7 pair narrows it. The net effect of these two opposing helical conformations is to facilitate divergence from stem III and toward the uridine turn. Together, these two rather different noncanonical AU base pairs therefore act to accommodate the three-stranded junction (Figures 2c and 3). The phosphodiester backbone chains leaving stem III and the stem II augmented helix in turn continue into the active site cytosine and the uridine turn, respectively, and then both finally come together to form stem I.

The A15.1–U16.1 base pair of stem III is absolutely conserved, suggesting that the broadening of the minor groove is crucial to catalytic activity. Replacement with a GC pair in either orientation or a UA pair in the opposite orientation abolishes activity (Ruffner et al., 1990). The GC substitution effect may be understood in terms of the greater propensity of the GC pair to establish a conventional 3-hydrogen bond Watson–Crick interaction rather than a 1-hydrogen bond interaction required to maintain the configuration of the minor groove in the region adjacent to the active site. The orientational requirement for the

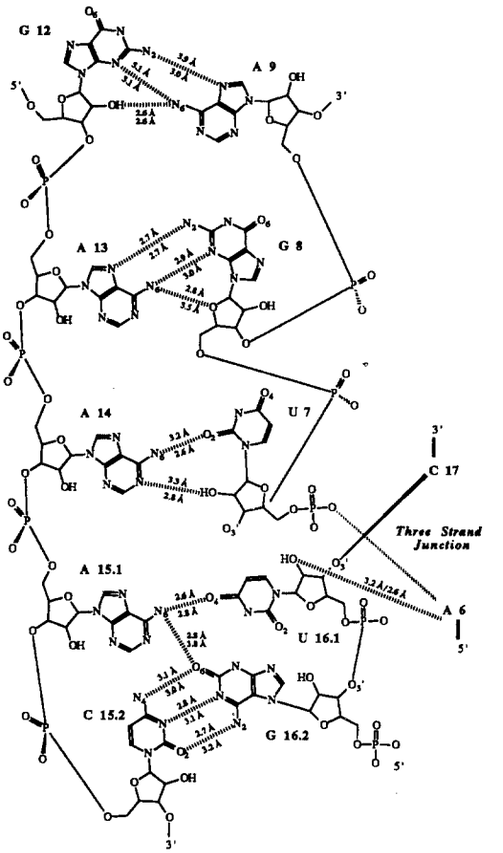

Figure 3. A Highly Schematic Diagram of the Mostly Conserved Base Pairs of the Augmented Stem II Helix, Which Together with the Conserved Bases of the Stem III Helix as Well as Flanking Residues C17 and A6 Illustrates the Structure of the Three-Stranded Junction

Hydrogen bonding distances are shown, including those of the reversed-Hoogsteen base pairs (G12 with A9 and A13 with G8). In molecule one, the G12–A9 interaction appears to be weakened compared with that in molecule two and the three molecules of the previous structure. Details of the base pairing scheme are described in the text. Note especially the single hydrogen bonds between the AU pairs and the bifurcated hydrogen bond in stem III. Distances for molecule one are shown above those for molecule two.

A15.1–U16.1 base pair may be explained by our observation that the exocyclic amine of A15.1 forms a bifurcated hydrogen bond (Figure 3), interacting with the exocyclic oxygen of G16.2 in the adjacent base pair of stem III. This bifurcated hydrogen bond also explains the preference for a G or at least a purine in the 16.2 position of stem III.

The branching architecture of stem I and the conformation of the three-strand junction are further stabilized by a number of true long-range RNA tertiary interactions, some of which could not be observed in the RNA–DNA hybrid ribozyme structure. These include the set of hydrogen bonds illustrated schematically as pink broken lines in Figure 2c. The hydrogen bonds between the 2′-hydroxyls of U16.1 and A6 as well as between the O2 of U16.1 and the 2′-hydroxyl of A6, between O4 of U7 and the 2′-hydroxyl of U16.1, and finally between the 2′-

hydroxyls of C15.2 and G5 act in a coordinated manner to fix the augmented stem II helix to stem III and to fix the catalytic pocket to stem III. The rigidity of this structure imposed by the long-range hydrogen-bonding interactions in turn defines the position of stem I relative to the long helix formed by the augmented stem II helix and stem III. Also, the approximately 100-fold preference for an all-RNA substrate over an analogous DNA substrate with a ribonucleotide in the active site (Dahm and Uhlenbeck, 1990; Pley et al., 1994) may be understood in part by the presence of hydrogen bonds involving the 2′-OH of U16.1. These interactions are not only likely to facilitate substrate interaction with the active site (especially in the uridine turn), but also may compensate energetically for the lack of a hydrogen bond between the N1 of A15.1 and the N3 of U16.1 in stem III. The lack of this 2′-hydroxyl in the DNA substrate analog thus eliminates some stabilizing hydrogen-bonding interactions. Together with the inherently greater instability of a DNA–RNA duplex, this observation accounts for at least part of the difference in substrate affinity between the ribozyme–DNA complex and the ribozyme–RNA complex.

The Conserved Uridine Turn and the Catalytic Pocket of the Ribozyme Cleavage Site

The uridine turn consists of the loop of four nucleotides (C3–U4–G5–A6) that smoothly connects stem I to the augmented helix of stem II by bending the enzyme strand of the molecule, and it is located directly opposite to the substrate strand cleavage site. As has been previously noted (Pley et al., 1994), this loop of four nucleotides is very similar in conformation to the uridine turn found in the tRNA anticodon loop (Robertus et al., 1974; Kim et al., 1974). The A6–U7 junction that connects the uridine turn to the augmented helix of stem II crosses the substrate strand backbone between the active site C17 and the conserved U16.1 of stem III, insinuating itself between the latter two bases, effectively splaying them apart. This has the effect of separating C17 from the augmented helix of stem II as the latter stacks upon stem III. Although this interaction contorts the sugar–phosphate backbone between C17 and U16.1, it is not this bond but the phosphodiester bond 3′ to C17 that is cleaved. This latter bond (the scissile bond) most likely becomes activated by a metal bound in the catalytic pocket.

An important structural feature is the presence of aromatic interactions that stabilize the conformation of the catalytic pocket. In addition to the hydrogen bond that stabilizes the active site cytosine, two aromatic interactions in the catalytic pocket between the active site base and the conserved uridine turn add additional stabilization to C17; these are depicted schematically as green broken lines in Figure 2c and in more detail in Figure 4a. One of these aromatic interactions is the perpendicular stacking interaction between the furanose oxygen of C17 and the platform formed by the base of A6. This interaction is reminiscent of that described in Z-DNA between the guanine base in the *syn* position that stacks on the furanose oxygen of the adjacent cytosine (Wang et al., 1979). The other is a stacking interaction between the base of C17 and the exocyclic O2 of U4 in the uridine turn, which makes a 3 Å aromatic-nπ-stabilizing interaction of the type previously described in protein enzyme active sites (Thomas et al., 1982; Burley and Petsko, 1985) and nucleotide crystals (Bugg et al., 1971). These interactions are significant not only because they can in principle stabilize any base at the active site, but also because they may allow sufficient flexibility to stabilize the active site base throughout the catalytic reaction pathway, a point invoked in our discussion of possible cleavage mechanisms, below.

Finally, the requirement that the four nucleotides of the uridine turn be absolutely conserved for catalytic activity (Ruffner et al., 1990) may best be understood in terms of both structure and function. C3, and possibly U4, may function primarily to bind the catalytic metal ion as described below in our discussion of a proposed mechanism. U4 also is capable of stabilizing interactions with the active site base as discussed previously. G5 and A6 function together as a stable purine-dominated stacking platform that interacts with the active site base furanose oxygen and may also be available for transition-state stabilization (as discussed in the proposed mechanism and illustrated in Figure 5B). These bases facilitate formation of the turn that allows the loop of four nucleotides to connect to stem III. Conservation of the CUGA sequence is also probably required to prevent formation of an alternative and presumably inactive GNRA- or UUCG-type tetraloop conformation in place of that required for catalytic activity.

Solvent Structure and Possible Metal-Binding Sites

An advantage of using crystals of the hammerhead RNA obtained from a relatively low concentration of ammonium salts is that competition with $Mg(H_2O)_6^{2+}$ for specific binding sites is less likely to be a problem than with the previous crystals, which were obtained in 2 M Li_2SO_4 or $(NH_4)_2SO_4$ (Pley et al., 1994). In fact, we can identify five potential Mg(II)-binding sites among the various solvent peaks that are visible in both the refined electron density map and difference Fourier maps computed with refined phases; the first four appear in both crystallographically independent molecules. Site 2 corresponds to a Mn(II) site identified in stem II of the previous hammerhead RNA structure, and site 3 is positioned near the ribozyme catalytic pocket. Although the X-ray scattering data by themselves cannot confirm the identity of a solvent peak, solvent peaks may be assigned as potential $Mg(H_2O)_n^{2+}$ sites upon the basis of stereochemical constraints. The optimal distance between a water oxygen atom and a hydrogen bond acceptor, for example, is approximately 2.8 Å, whereas the distance between a Mg^{2+} and a bound oxygen (either a phosphate oxygen or a hydrating water oxygen) is 2.05 Å. Therefore, a solvent peak assigned as a Mg^{2+} bound directly to a phosphate oxygen should be centered about 2.05 Å from the phosphate oxygen, and a solvent peak corresponding to a fully hydrated $Mg(H_2O)_6^{2+}$ will in general be between 3.5 Å and 5.0 Å from its nearest neighbor, depending upon its orientation. These criteria have al-

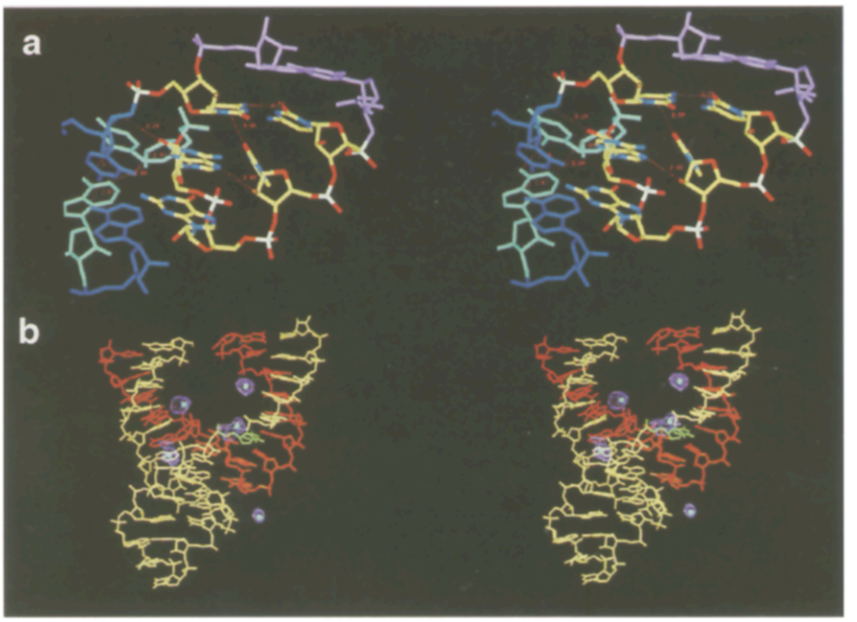

Figure 4. The Hammerhead Ribozyme Catalytic Pocket and Metal-Binding Sites

(a) A stereo view of the hammerhead ribozyme catalytic pocket and flanking regions found in the first molecule in the asymmetric unit of our crystal is shown. The uridine turn (C3–U4–G5–A6) and the active site cytosine (C17) are shown as a color-coded stick model (yellow, carbon; white, phosphorous; red, oxygen; blue, nitrogen). The flanking stem I base pair (A1.1–U2.1) is shown in magenta, and the two flanking non-Watson–Crick base pairs of stem III and the augmented stem II helix are shown in dark and light blue, respectively. Hydrogen bonds and the U4–C17 interaction are marked with distances in angstroms in red. Note that aromatic stabilization interactions occur between the furanose oxygen of C17 and the base of A6 and between the exocyclic oxygen of U4 and the base of C17.

(b) Stereo diagram illustrating the five potential magnesium-binding sites. The enzyme and substrate analog strands are shown in red and yellow, respectively, with the active site base shown in green. Five solvent difference Fourier peaks that cannot be assigned as water sites are shown in magenta, contoured at 2.8 σ. These have been assigned as hydrated $Mg(H_2O)_n^{2+}$ complex ion sites as described in the text, according to stereochemical criteria that are summarized there and in Table 2. Site 1 is located on stem I; site 2 is on stem II and is essentially the same as the Mn(II) site observed in the previous hammerhead structure. Site 3 is the only solvent peak near the active site base and the catalytic pocket, and sites 4 and 5 are associated with stem III. The refined positions of the five Mg(II) cations are indicated by light blue spheres.

lowed us to identify five potential $Mg(H_2O)_n^{2+}$ sites, which are listed in Table 2, together with the interatomic distances between each of them and their nearest neighbors. The location of the five potential Mg(II) sites is shown in Figure 4b.

The most prominent of these peaks, corresponding to site 1, is quite pronounced in the initial multiple isomorphous replacement and anomalous scattering (MIRAS) map (even before symmetry averaging was applied to improve phases) and persists throughout the refinement. This solvent peak most likely corresponds to $Mg(H_2O)_6^{2+}$ bound to the O6 and N7 functional groups of the adjacent guanines at positions 2.2 and 2.3 in stem I. These bases are in the nonconserved region of the hammerhead RNA, so it is unlikely that this $Mg(H_2O)_6^{2+}$ site is critical to the function of the ribozyme.

The second most prominent peak, corresponding to site 2, very likely corresponds to $Mg(H_2O)_5^{2+}$ bound directly to the pro-S oxygen of A9 and associated via the hydration shell with the exocyclic oxygen O6 of G8, the N7 of G10.1, and the N2 of G12. This potential $Mg(H_2O)_5^{2+}$ site, equally prominent in both hammerhead RNA molecules in the asymmetric unit, corresponds quite closely to a Mn(II) site identified by Pley et al. (1994) in hammerhead crystals soaked in 100 mM $MnCl_2$. However, Mn(II) binds to the pro-R oxygen of A9 in the previous structure. That the location of this Mg(II) site is in the conserved region of the augmented stem II helix suggests that the G10.1–C11.1 base pair is conserved in this orientation to preserve the integrity of $Mg(H_2O)_5^{2+}$ binding at this site and that G12 may be conserved for this reason (as well as others) also. The fact that this site is very similar to the Mn(II) site in the previous structure adds credibility to its identification as a Mg(II) site and also suggests that the absence of Mg(II) at this site (and possibly at the other four sites) in the previous hammerhead structure is likely due to competition from the high concentration of monovalent cations in the previous crystallization condition.

The third potential $Mg(H_2O)_6^{2+}$ site, corresponding to site 3 in Table 2, is somewhat less prominent than the first two but does appear almost equally strong in both hammerhead RNA molecules of the asymmetric unit of the crystal. This solvent peak is associated with several of the conserved bases in the catalytic pocket, including the exocyclic amine of C3 in the uridine turn and the exocyclic amine of C17, the cleavage site base. Removal of either

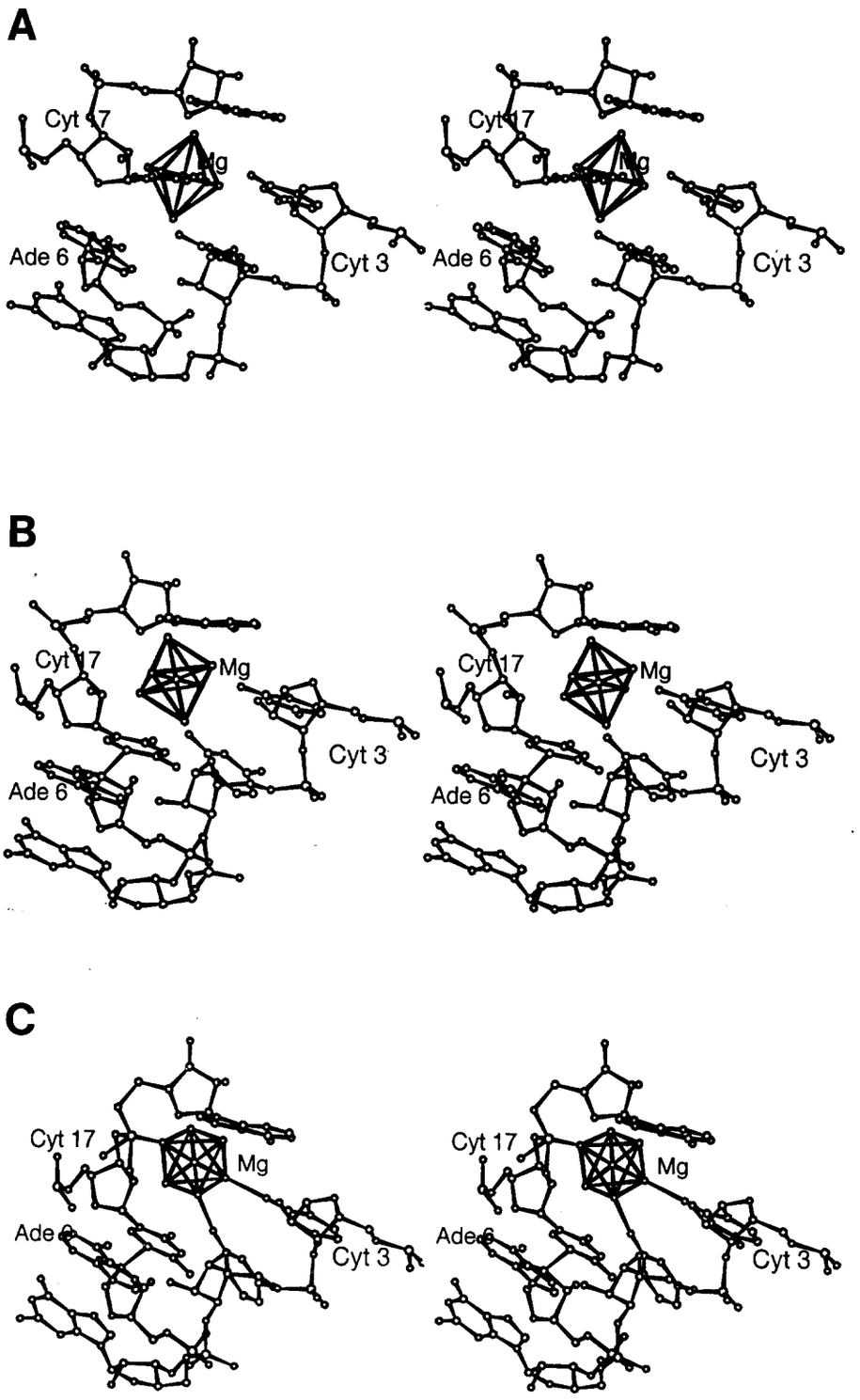

Figure 5. Three Possible Points in the Proposed Hammerhead Ribozyme Self-Cleavage Reaction Pathway as Described in the Text

(A) The first is based upon Mg(II) site 3 found in the difference Fourier map of the ribozyme structure. In this first step, $Mg(H_2O)_6^{2+}$ (represented as an octahedron) is coordinated primarily by the exocyclic amine of C3 in the catalytic pocket, as well as by C17.

(B) At the second point, the $Mg(H_2O)_6^{2+}$ is moved inward closer to the active site cytosine 2′-hydroxyl, and the base of C17 is shown pivoting downward slightly to stack upon the purine platform formed by G5 and A6 of the catalytic pocket. This second site is identical to that found for $Mg(H_2O)_6$ binding in the uridine turn of $tRNA^{Phe}$.

(C) The small low energy conformational changes of the catalytic pocket now allow the Mg(II) to move still closer into the active site to activate catalysis, as shown in (C), where this third postulated Mg(II) position is based on the Pb(II)-binding position in $tRNA^{Phe}$, and the geometry depicted approximates that of the pentacoordinated phosphate intermediate or transition state. The solvated Mg(II) has been relayed from the exocyclic amine of C3 to the exocyclic oxygen, positioning it for attack at the 2′-hydroxyl of the active site nucleotide. A detailed description of this mechanism is presented in the text.

Table 2. Potential $Mg(H_2O)_n$ Sites with Nearest Neighbor Distances

$Mg(H_2O)_n$ Site	Nearest Neighbors		Molecule One (Å)	Molecule Two (Å)
Site 1	GUA 2.2	N7	3.8	4.1
		O6	4.8	3.7
	GUA 2.3	N7	4.6	4.5
		O6	4.7	4.5
Site 2	GUA 8	O2′	3.8	3.8
	ADE 9	O1P	2.1	2.0
	GUA10.1	N7	3.9	3.3
	GUA 12	N2	4.6	4.7
Site 3	ADE 1.1	N6	4.7	4.7
	CYT 3	N4	4.5	4.9
	URA 4	O4	–	3.6
	URA 7	OP1	3.8	3.8
		OP2	4.0	3.4
	GUA 8	O2P	4.7	–
	CYT 17	N4	4.5	3.6
Site 4	GUA 8	O6	–	3.9
	URA 16.1	O4	–	4.0
	GUA 16.2	N7	4.4	4.2
		O6	4.6	4.5
	ADE 16.3	N7	4.2	–
		O2P	4.4	–
Site 5	GUA 5	O2P	–	4.4
	URA 15.3	O3′	–	5.0
	CYT 15.4	O1P	–	5.2

Approximate mean coordinate error is 0.35 Å.

of these exocyclic amines causes the dissociation constant for the catalytic $Mg(H_2O)_6^{2+}$ to increase by almost an order of magnitude, strongly suggesting that site 3 has been assigned correctly as a $Mg(H_2O)_6^{2+}$ (Murray et al., 1995). In addition, this potential $Mg(H_2O)_6^{2+}$ makes contacts with the exocyclic amine of A1.1, a nonconserved residue in stem I, the phosphate oxygens of U7 in the augmented stem II helix, the exocyclic O4 of U4 (only in molecule 2), and a phosphate oxygen in G8 (only in molecule 1). Because site 3 is the only solvent peak located near the catalytic pocket of the hammerhead ribozyme, a discussion of its mechanistic implications is provided in the proposed mechanism section below. Site 3, like site 2, reappears in crystals soaked in 70 mM $MnCl_2$ prior to data collection. Site 3 and the remaining two sites are further summarized in Table 2.

Metal Binding Properties of the Homologous $tRNA^{Phe}$ Uridine Turn

The presence of the absolutely conserved CUGA uridine turn in the catalytic pocket of the hammerhead ribozyme in a conformation virtually identical to that found in the uridine turn of the anticodon loop of $tRNA^{Phe}$ indicates that this structural element must play a role crucial to the mechanism of ribozyme catalysis. In tRNA, the relatively rigid structure of the uridine turn helps to position the anticodon triplet within the loop in a conformation suitable for recognizing a messenger RNA codon. In addition, the uridine turn, in conjunction with other bases in the anticodon loop, binds a variety of divalent metal ions, including Mg(II) and Pb(II). The fact that the uridine turn can function as a permissive metal-binding pocket in tRNA strongly suggests that it plays a similar role in mediating divalent metal ion cleavage of RNA in the hammerhead ribozyme. The hammerhead ribozyme indeed permits a wide variety of divalent cations to assist in substrate strand cleavage, including Mg(II), Mn(II), Co(II), Ca(II), Cd(II), Sr(II), and Zn(II) (Dahm and Uhlenbeck, 1991). The ability of the catalytic site of the hammerhead ribozyme to accommodate a variety of divalent metal ions is of obvious importance; thus, the permissive metal-binding capabilities of the uridine loop structure shared between tRNA and hammerhead RNA is particularly suggestive.

A very clear solvent peak, located near Cm32 in the four nucleotide uridine turn of the anticodon loop in the monoclinic form of $tRNA^{Phe}$ (Jack et al., 1977), appears more prominently in the orthorhombic form of $tRNA^{Phe}$, which was crystallized in the presence of 40 mM $MgCl_2$. This peak has been assigned as one of four strong Mg^{2+}-binding sites in the latter crystal form (Holbrook et al., 1977). This Mg^{2+} is directly coordinated with one of the phosphate oxygens of residue 37 and forms a water-mediated hydrogen bond to Cm32. In addition, the monoclinic form of tRNA is found to bind Pb(II) in a similar manner within the anticodon loop, again adjacent to Cm32 in the uridine turn, in a position rather close to that of the Mg^{2+} found in the orthorhombic crystal form of tRNA (Brown et al., 1983, 1985).

The Cm32 residue of the uridine turn in tRNA corresponds to C3 in the uridine turn catalytic pocket of the

hammerhead ribozyme; C3 is in fact located directly opposite to and within hydrogen-bonding distance of the cytosine, C17, at the cleavage site. In fact, a superposition of these two metal-binding sites in the uridine turn of $tRNA^{Phe}$ with the virtually identical uridine turn of the hammerhead RNA structure aligns the Mg(II) and Pb(II) of $tRNA^{Phe}$ quite close to the active site base, C17, of the hammerhead RNA. This alignment, used to generate Figure 5, suggests that the uridine turn of the hammerhead ribozyme is in fact capable of binding Mg(II) hexahydrate in a location proximal to the scissile bond of the substrate, i.e., at one of the unsatisfied hydrogen bond potential donors of C3. A mechanism for hammerhead cleavage, based upon the potential Mg(II) hexahydrate identified as site 3, as well as upon the alignment of the metal-binding sites in the uridine turn of tRNA with the catalytic pocket of the hammerhead ribozyme, is presented in the following section.

A Proposed Mechanism for Hammerhead Ribozyme Catalytic Cleavage

The only solvent peak visible near the catalytic pocket of the hammerhead ribozyme is the one we have assigned as magnesium site 3. It is positioned near C17 and C3 of the uridine turn (Figures 4b and 5A; Table 2), but is not quite within striking distance of the 2′-oxygen of the active site furanose. It is possible that this is due to the presence of the 2′-O-methyl moiety, which likely disrupts proper metal binding. Comparison with the $Mg(H_2O)_5^{2+}$ site found in the uridine turn of the anticodon loop of $tRNA^{Phe}$ and the $Pb(H_2O)_n^{2+}$ site similarly located in tRNA suggests how the position of the metal might change slightly in the absence of the 2′-O-methyl modification and allows us to construct plausible models of three consecutive points in the proposed pathway of the catalytic reaction.

The first point in the reaction pathway is based upon the observed difference Fourier peak, shown in Figure 4b, which we have assigned as a $Mg(H_2O)_6^{2+}$ that binds to the exocyclic amine of C3 in the uridine turn. This binding event positions the complex ion conveniently for a direct approach to the scissile phosphodiester bond between C17 and the adjacent A1.1 of stem I. This first point in the reaction pathway is illustrated in Figure 5A and is corroborated by cytosine modification studies that demonstrate that the catalytic Mg(II) binds to the exocyclic amines of C3 and C17 (Murray et al., 1995). Thus, the proposed initial Mg(II)-binding event in this mechanism involves the exocyclic amines on C3 and C17 and predicts correctly that elimination of these exocyclic amines should have the effect of disrupting the initial Mg(II)-binding event.

The second point in the reaction pathway is based upon the crystal structure of $tRNA^{Phe}$ and the Mg(II) site near C32. The $Mg(H_2O)_6^{2+}$ moves 3.5 Å closer to the 2′-hydroxyl of C17 and the scissile bond. To do so, the bulky complex ion must be accommodated by a rotation of the glycosidic bond of C17 that causes the aromatic base itself, rather than the furanose oxygen of its ribose, to stack upon A6 of the uridine turn (which itself is stacked upon G5), as shown in Figure 5B. This new base-stacking interaction stabilizes the new conformation C17 at the expense of placing additional strain upon the scissile phosphodiester bond. The widening gap between the bases of C17 and A1.1 accommodates the $Mg(H_2O)_6^{2+}$ as it now moves still closer to the 2′-hydroxyl of C17 and the scissile bond.

At the third point in the proposed reaction pathway, which is based upon comparison with the crystal structure of $tRNA^{Phe}$ and the Pb(II) site near $tRNA^{Phe}$ C32, the hydrated magnesium ion is close enough to abstract a proton from the 2′-hydroxyl of C17 and initiate the cleavage reaction. The third step, with the hydrated divalent metal now bound to the exocyclic oxygen of C3 (and possibly in addition to that of U4) in the uridine turn, is shown in Figure 5C, together with a concomitant formation of the pentacoordinated cyclic phosphate intermediate or transition state. In-line attack of the nucleophile is postulated in the proposed mechanism to be consistent with the available experimental data (van Tol et al., 1990; Slim and Gait, 1991; Koizumi and Ohtsuka, 1991). Insertion of the hydrated magnesium complex ion causes strain upon the scissile phosphodiester bond and facilitates strand separation during or subsequent to the cleavage reaction. In Figure 5C, the magnesium is directly coordinated to the pro-R oxygen, which requires the local rearrangement in the phosphate backbone shown. However, a solvated water molecule may also make the contact to the phosphate oxygen, as previously suggested (Koizumi and Ohtsuka, 1991), making such a conformational adjustment unnecessary.

Although we believe this to be a reasonable and detailed hypothesis that makes specific and testable predictions and one that is supported by two types of RNA crystal structure, the definitive elucidation of the hammerhead ribozyme cleavage mechanism must be based upon direct high resolution dynamic experiments. We are currently attempting to test the validity of our proposed ribozyme cleavage mechanism with several such experiments to elucidate further the role of divalent metal ions in hammerhead RNA catalysis.

Experimental Procedures

Crystallization

Crystals of RNA6 were prepared as described elsewhere (Scott et al., 1995). In brief, each of the RNA strands was synthesized by use of oligoribonucleotide phosphoramidite chemistry, incorporating a 2′-O-methyl cytosine in the active site of the substrate RNA strand. Purified ribozyme complex (0.5 mM) in 10 mM ammonium cacodylate (pH 6.5) was combined with an equal volume (2–10 μl) of reservoir solution (50 mM ammonium cacodylate, 100 mM NH_4OAc, 10 mM $Mg(OAc)_2$, 1 mM spermine, 23% PEG 6000, and 5% glycerol) and equilibrated as a sitting drop against the reservoir solution at 20°C. Crystals formed in the space group $P3_121$, with cell dimensions a = b = 64.9 Å, c = 138.1 Å. Two derivative crystals were prepared identically to the native crystals but using 5-BrdU phosphoramidites at positions 2.1 and 2.4 in the syntheses of the substituted enzyme strands.

Data Collection and Solution of Structure

Both native and derivative data were collected at Daresbury Laboratory (Warrington, England) synchrotron beamline 9.6 by using 0.882 Å X-rays and a MAR imaging plate detector on crystals frozen at 100°K in the reservoir solution containing 25% glycerol as a cryoprotectant. Anomalous scattering data were collected for both bromine derivatives. The images were processed by MOSFLM (A. G. W. Leslie, Medical Research Council Laboratory of Molecular Biology, Cambridge, England), and standard crystallographic computations were carried out within the CCP4 program suite (Collaborative Computational Proj-

ect Number 4, 1994). Isomorphous and anomalous difference Patterson maps were interpreted with the aid of SHELX-90 (Sheldrick, 1991) and cross-checked with difference Fourier maps. The space group enantiomorph was determined, and phases were computed with MLPHARE (Otwinowski, 1991) and subsequently were subjected to solvent-flattening refinement using an estimated solvent content of 0.4 (Wang, 1985). A 3.1 Å electron density MIRAS map was calculated within CCP4 and interpreted by using the graphics display program O (version 5.8.1; T. A. Jones and M. Kjeldgaard, Uppsala University, Uppsala, Sweden) with the aid of standard A-form model helices of stems I, II, and III, generated by using the Biopolymer module of INSIGHT II (Version 2.2.0; Biosym Technologies, San Diego, CA). The initial map revealed clear helical regions and allowed complete tracing of two molecules in the asymmetric unit. The two independent copies of stem I were readily located in the electron density from the positions of the bromine atoms in the derivative structures. This allowed the adjacent stem II and stem III with its tetraloop to be positioned in each of the two molecules. Finally, the central core and the uridine turn in each molecule were located and built into place. A 2-fold averaged MIRAS map generated by using a solvent mask from one of the molecules in the asymmetric unit with the symmetry-averaging and solvent-flattening program Solomon (Abrahams et al., 1994) verified the chain tracing and greatly improved the quality of the map. The completed initial model was refined both with and without a noncrystallographic symmetry harmonic restraint using a standard simulated annealing slow-cooling molecular dynamics protocol followed by conventional positional and restrained temperature factor refinement in X-PLOR (version 3.1 [1993]; A. T. Brünger, Howard Hughes Medical Institute and Department of Molecular Biophysics and Biochemistry, Yale University, New Haven, CT), giving an R factor of about 27% in the presence of the noncrystallographic restraint and 25% in its absence. Details of the refinement statistics are listed in Table 1. Each subsequent round of refinement was followed by inspection of the MIRAS map as well as $2F_o$-F_c and F_o-F_c maps generated in X-PLOR 3.1 and manual readjustment of the model.

Availability of Coordinates

Coordinates will be deposited in the Brookhaven data base. While these are being processed, they may be obtained via electronic mail from wgs@mrc-lmb.cam.ac.uk.

Acknowledgments

We thank Michael Gait, Stephen Price, Chris Oubridge, Kiyoshi Nagai, Jane Grasby, and the oligonucleotide synthesis service at the Medical Research Council Laboratory of Molecular Biology for advice and assistance in preparing the RNA samples. We also thank Phil Evans, Gabriele Varani, Stephen Price, and the other staff of the Structural Studies Division for useful advice and numerous helpful discussions, and we thank David McKay and his coworkers for discussing with us their ribozyme structure and for providing us with coordinates of their hammerhead ribozyme molecule two. Finally, we thank the three reviewers of this manuscript for their helpful critique of the first version, and Olke Uhlenbeck for his helpful and enthusiastic advice in preparing this paper. W. G. S. thanks the American Cancer Society for a postdoctoral fellowship (grant number PF-3970).

Received March 13, 1995; revised April 25, 1995.

References

Abrahams, J. P., Leslie, A. G. W., Lutter, R., and Walker, J. E. (1994). The structure of F1-ATPase from bovine heart mitochondria determined at 2.85 Å resolution. Nature *370*, 621–628.

Barinaga, M. (1993). Ribozymes: killing the messenger. Science *262*, 1512–1514.

Brown, R. S., Hingerty, B. E., Dewan, J. C., and Klug, A. (1983). Pb(II)-catalysed cleavage of the sugar–phosphate backbone of yeast $tRNA^{Phe}$: implications for lead toxicity and self-splicing RNA. Nature *303*, 543–546.

Brown, R. S., Dewan, J. C., and Klug, A. (1985). Crystallographic and biochemical investigation of the lead(II)-catalyzed hydrolysis of yeast phenylalanine tRNA. Biochemistry *24*, 4785–4801.

Bugg, C. E., Thomas, J. M., Sundaralingam, M., and Rao, S. T. (1971). Stereochemistry of nucleic acids and their constituents. X. Solid-state base-stacking patterns in nucleic acids and polypeptides. Biopolymers *10*, 175–219.

Burley, S. K., and Petsko, G. A. (1985). Aromatic–aromatic interaction: a mechanism of protein structure stabilization. Science *229*, 23–28.

Cech, T. R. (1990). Self-splicing of group I introns. Annu. Rev. Biochem. *59*, 543–568.

Collaborative Computational Project Number 4 (1994). The CCP4 suite: programs for protein crystallography. Acta Cryst. *D50*, 760–763.

Dahm, S. C., and Uhlenbeck, O. C. (1990). Characterization of deoxy- and ribo-containing oligonucleotide substrates in the hammerhead self-cleavage reaction. Biochemie *72*, 819–823.

Dahm, S., and Uhlenbeck, O. C. (1991). Role of divalent metal ions in the hammerhead RNA cleavage reaction. Biochemistry *30*, 9464–9469.

Dahm, S., Derrick, W. B., and Uhlenbeck, O. C. (1993). Evidence for the role of solvated metal hydroxide in the hammerhead cleavage mechanism. Biochemistry *32*, 13040–13045.

Gait, M. J., Pritchard, C., and Slim, G. (1991). Oligoribonucleotide synthesis. In Oligonucleotide Synthesis: A Practical Approach, F. Eckstein, ed. (Oxford: Oxford University Press), pp. 25–48.

Gesteland, R. F., and Atkins, J. F., eds. (1993). The RNA World: The Nature of Modern RNA Suggests a Prebiotic RNA World (Cold Spring Harbor, New York: Cold Spring Harbor Laboratory Press).

Gopalan, V., Talbot, S. J., and Altman, S. (1994). RNA–protein interactions in RNase P. In RNA–Protein Interactions, K. Nagai and I. W. Mattaj, eds. (Oxford: Oxford University Press), pp. 103–126.

Holbrook, S. R., Sussman, J. L., Warrant, R. W., Church, G. M., and Kim, S.-H. (1977). RNA–ligand interactions. I. Magnesium binding sites in yeast $tRNA^{Phe}$. Nucl. Acids Res. *8*, 2811–2820.

Jack, A., Ladner, J. E., Rhodes, D., Brown, R. S., and Klug, A. (1977). A crystallographic study of metal-binding to yeast phenylalanine transfer RNA. J. Mol. Biol. *111*, 315–328.

Kim, S.-H., Suddath, F. L., Quigley, G. J., McPherson, A., Sussman, J. L., Wang, A. H. J., Seeman, N. C., and Rich, A. (1974). Three-dimensional tertiary structure of yeast phenylalanine transfer RNA. Science *185*, 435–440.

Koizumi, M., and Ohtsuka, E. (1991). Effects of phosphorothioate and 2-amino groups in hammerhead ribozymes on cleavage rates and Mg^{2+} binding. Biochemistry *30*, 5145–5150.

Murray, J. B., Adams, C. J., Arnold, J. R. P., and Stockley, P. G. (1995). The roles of the conserved pyrimidine bases in hammerhead ribozyme catalysis. Biochem. J., in press.

Otwinowski, Z. (1991). Maximum likelihood refinement of heavy atom parameters. In Isomorphous Replacement and Anomalous Scattering: Proceedings of the CCP4 Study Weekend, W. Wolf, P. R. Evans, and A. G. W. Leslie, eds. (Warrington, England: Daresbury Laboratory), pp. 80–86.

Pley, H. W., Flaherty, K. M., and McKay, D. B. (1994). Three-dimensional structure of a hammerhead ribozyme. Nature *372*, 68–74.

Robertus, J. D., Ladner, J. E., Finch, J. T., Rhodes, D., Brown, R. S., Clark, B. F. C., and Klug, A. (1974). Structure of yeast phenylalanine tRNA at 3 Å resolution. Nature *250*, 546–551.

Ruffner, D. E., Stormo, G. D., and Uhlenbeck, O. C. (1990). Sequence requirements of the hammerhead RNA self-cleavage reaction. Biochemistry *29*, 10695–10702.

Schultz, S. C., Shields, G. C., and Steitz, T. A. (1991). Crystal structure of a CAP–DNA complex: the DNA is bent by 90°. Science *253*, 1001–1007.

Scott, W. G., Finch, J. T., Grenfell, R., Fogg, J., Smith, T., Gait, M. J., and Klug, A. (1995). Rapid crystallization of chemically synthesized "hammerhead" RNAs using a "double screening" procedure. J. Mol. Biol., in press.

Sheldrick, G. M. (1991). Heavy atom location using SHELXS-90. In Isomorphous Replacement and Anomalous Scattering: Proceedings

of the CCP4 Study Weekend, W. Wolf, P. R. Evans, and A. G. W. Leslie, eds. (Warrington, England: Daresbury Laboratory), pp. 23–28.

Slim, G., and Gait, M. J. (1991). Configurationally defined phosphorothioate-containing oligoribonucleotides in the study of the mechanism of cleavage of hammerhead ribozymes. Nucl. Acids Res. *19*, 1183–1188.

Sullenger, B. A., and Cech, T. R. (1993). Tethering ribozymes to a retroviral packaging signal for destruction of viral RNA. Science *262*, 1566–1569.

Symons, R. H. (1992). Small catalytic RNAs. Annu. Rev. Biochem. *61*, 641–671.

Thomas, K. A., Smith, G. M., Thomas, T. B., and Feldman, R. J. (1982). Electronic distributions within protein phenylalanine aromatic rings are reflected by the three-dimensional oxygen atom environments. Proc. Natl. Acad. Sci. USA *79*, 4843–4847.

Taira, K., Uebayasi, M., Maeda, H., and Furukawa, K. (1990). Energetics of RNA cleavage: implications for the mechanism of action of ribozymes. Prot. Eng. *3*, 691–701.

Uhlenbeck, O. C. (1987). A small catalytic oligoribonucleotide. Nature *328*, 596–600.

Usman, N., Ogilvie, K. K., Tiang, M.-Y., and Cedergren, R. G. (1987). Automated chemical synthesis of long oligoribonucleotides using 2′-O-silylated ribonucleotide 3′-O-phosphoramidites on a controlled glass support: synthesis of a 43 nucleotide sequence similar to the 3′-half molecule of an *Escherichia coli* formylmethionyl tRNA. J. Am. Chem. Soc. *109*, 7845–7854.

van Tol, H., Buzayan, J. M., Feldstein, P. A., Eckstein, F., and Bruening, G. (1990). Two autolytic processing reactions of a satellite RNA proceed with inversion of configuration. Nucl. Acids Res. *18*, 1971–1975.

Wang, A. H.-J., Quigley, G. J., Kolpak, F. J., Crawford, J. L., van Boom, J. H., van der Marel, G., and Rich, A. (1979). Molecular structure of a left-handed double helical DNA fragment at atomic resolution. Nature *282*, 680–686.

Wang, B. C. (1985). Resolution of phase ambiguity in macromolecular crystallography. Meth. Enzymol. *115*, 90–112.